Journal of Computational Physics **170,** 785–811 (2001)
doi:10.1006/jcph.2001.6762, available online at http://www.idealibrary.com on IDEAL®

Multigrid Solution of the Incompressible Navier–Stokes Equations for Density-Stratified Flow past Three-Dimensional Obstacles

M. F. Paisley

Department of Mathematics & Statistics, School of Computing, Staffordshire University, Stafford ST18 0AD, United Kingdom
E-mail: M.F.Paisley@staffs.ac.uk

Received August 27, 1999; revised November 14, 2000

The steady incompressible Navier–Stokes equations in three dimensions are solved for neutral and stably stratified flow past three-dimensional obstacles of increasing spanwise width. The continuous equations are approximated using a finite volume discretisation on staggered grids with a flux-limited monotonic scheme for the advective terms. The discrete equations which arise are solved using a nonlinear multigrid algorithm with up to four grid levels using the SIMPLE pressure correction method as smoother. When at its most effective the multigrid algorithm is demonstrated to yield convergence rates which are independent of the grid density. However, it is found that the asymptotic convergence rate depends on the choice of the limiter used for the advective terms of the density equation, and some commonly used schemes are investigated. The variation with obstacle width of the influence of the stratification on the flow field is described and the results of the three-dimensional computations are compared with those of the corresponding computation of flow over a two-dimensional obstacle (of effectively infinite width). Also given are the results of time-dependent computations for three-dimensional flows under conditions of strong static stability when lee-wave propagation is present and the multigrid algorithm is used to compute the flow at each time step.

Key Words: incompressible Navier–Stokes; multigrid; three dimensions; stratified flow; high-order schemes.

1. INTRODUCTION

The solution of the incompressible Navier–Stokes equations for flows past three-dimensional obstacles has important applications in many branches of fluid dynamics and beyond. This paper describes the recent development of a nonlinear multigrid algorithm for three-dimensional flows in finite depth with buoyancy effects and extends earlier work for stratified

0021-9991/01 $35.00

flows in two dimensions. The algorithm is capable of dealing with three-dimensional flows which may be neutral or density-stratified, steady or time-dependent, low or high Reynolds number, and in Cartesian or curvilinear geometry. Of the many methods proposed for generating solutions to the incompressible Navier–Stokes equations we continue to concentrate on the method of the finite volume formulation, which is appealing because of its relative simplicity and generality. Although the applications described here are primarily of meteorological interest, the procedures have wider relevance in the general area of numerical methods for incompressible flow.

Common to all implementations of the finite volume formulation is a conservative discrete approximation to the continuous steady-state equations, which may use staggered or collocated grids, and flux evaluations for advective terms on cell faces which may be limited in some manner to prevent unphysical effects. A convergent iterative procedure is then used to determine the solution to this set of discrete equations and these fall into several classes. Historically, the first is Chorin's [1] artificial compressibility method, whereby the time-dependent terms in the momentum equations are retained and a fictitious compressibility term is introduced into the continuity equation. This renders the system hyperbolic and an algorithm which advances the solution in pseudo-time to approach the steady state can be applied. For such problems time accuracy is unimportant and techniques such as preconditioning, local time-stepping, and multigrid can be used to accelerate convergence. For genuinely unsteady problems a dual time-stepping approach is adopted in which the physical time derivatives become source terms and the iteration in pseudo-time used to reach a steady state at each physical time step. See [2, 3] for recent applications with multigrid in three dimensions for steady and unsteady flow, respectively.

A second class of procedures consists of decoupled or segregated methods, dating back to Harlow and Welch [4] for unsteady flows and to Patankar [5] for steady flows, respectively. Starting from a given global pressure field the global velocity field is updated through the momentum equations. In pressure-based methods relationships between velocity and pressure corrections are used in the continuity equation to derive a Poisson equation for the pressure corrections with the current continuity residual on the right-hand side. Although originally implemented on staggered grids, similar schemes can be derived for collocated arrangements by the inclusion of appropriate additional terms [6]. Following the solution of this equation both pressure and velocity fields are updated globally and after the treatment of any other transport equations the iteration is repeated. Embedding the procedure within a nonlinear multigrid algorithm accelerates the convergence considerably [7–11]. The modifications required for unsteady flow are similar to those for artificial compressibility, where the time-derivative terms are included as modifications to the diagonal elements and the source terms of the discrete momentum equations, and the iteration seeks a steady solution at each time step. The recent comparison of the pressure-based approach with that of artificial compressibility for three-dimensional flows [12, 13] noted an efficiency disadvantage for the pressure correction method for steady flow and a gain for unsteady flow, although these conclusions applied only to the single-grid implementations investigated.

A third class of methods is similar to the second in that the steady-state equations are solved directly but with a solution procedure based on a coupling of the equation set. Vanka's SCGS (symmetric coupled Gauss–Seidel) method allied with a multigrid algorithm in two [14] and three dimensions [15] is the earliest example of this kind of approach. The convergence rates given by cellwise coupling deteriorate for high aspect ratio grids or aligned flow and coupling in lines [16, 17] is to be preferred. In both of these cases the

relatively simple matrix structure enables exact inversion, but these methods are likely to be inefficient if strong anisotropy is present in two spatial directions. Improvement may be gained by generalizing the approach to solving the fully coupled equation set over planes and employing algorithms such as Krylov subspace methods in combination with the multigrid [18–20].

A fourth class of algorithms consists of distributive relaxation methods such as DGS (distributive Gauss–Seidel) [21–23], where an equivalent system of equations is obtained in terms of new variables using a distribution operator. Gauss–Seidel relaxation is used for each equation for each new variable in turn, introducing the changes in the original variables implied by the distribution operator. This means that following the usual relaxation of the momentum equations the continuity equation is relaxed by changing several values together.

The approach taken here is a straightforward extension of that described in [10], where the primitive variables are defined on staggered grids and the discrete equations which arise from the finite volume formulation are solved using a nonlinear multigrid method with an appropriate smoother. The issue of the choice of smoother was addressed in [24], where a comparison was made of multigrid computation of flow over two-dimensional obstacles as well as the test problem of the two-dimensional lid-driven cavity. The computing times for the coupled methods SCGS [14] and CLGS (collective line Gauss–Seidel) [16] were compared with those of the SIMPLE (semi-implicit method for pressure linked equations) [5] pressure correction smoother. Although the coupled methods were faster for the two-dimensional cavity, concurring with [25, 26], the converse was found to be the case for the flow over the two-dimensional obstacles. A recent comparison of the three-dimensional lid-driven cavity [27] with the two-dimensional cavity drew the same conclusion, and the line-coupled method was optimal.

The smoother used here is the SIMPLE pressure correction method, because early numerical experiments suggested that it was faster for three-dimensional flows over obstacles than the coupled line smoother CLGS. (It may be that CLGS is not the best available—the algorithm [17], for example, appears well suited to inflow–outflow as well as recirculating flow problems, although comparison with it is outside the scope of this paper.) The performance of SIMPLE for these three-dimensional flows is compared with that observed when used for the corresponding two-dimensional problem. The benefit of multigrid, in terms of a reduction in computing time over the corresponding single grid computation, increases with grid size (the number of nodes). It is a matter of practical interest to determine what might be expected in three dimensions given that the grid sizes tend to be smaller in each direction.

The main focus of the paper, however, is the computation of density-stratified flow, requiring the addition of a scalar density transport equation and corresponding buoyancy term in the vertical momentum equation. Because the Schmidt number (the ratio of viscous to diffusive effects) varies according to the fluid under consideration, a robust multigrid algorithm which converges well is required, particularly for convection-dominated problems. In addition, it is well known that unless a flux-limited scheme is implemented, undershoots can occur and may lead to unphysical phenomena such as negative densities. Prior to the work described here, only one kind of limiter had been used and although no convergence difficulties had been encountered in neutral flow, it was noticed that asymptotic convergence was often harder to obtain in stratified flow. Remedies suggested in [24] included using a double discretisation, whereby the high-order part of the scheme was not included in the

iteration on the coarser grids. Although this improved the asymptotic convergence in the two-dimensional flows tried, it did not appear to help with subsequent initial computations of stratified flow in three dimensions. This prompted the investigation of several well-known limiter functions on convergence rates which is included here. The best of these is then deployed in the multigrid algorithm to compute steady flow over the three-dimensional barriers under conditions of neutral and stable stratification.

Some results were given in [10] for unsteady flows using the kind of approach described. That is, a steady problem is solved at each time step, with the flow at the previous time step regarded as the initial condition for the flow at the new time step. The set of changes in the solution sought at each time step consists of high-frequency information and the multigrid algorithm is not expected to be as effective in the individual steps of an unsteady computation as when employed to determine a steady state solution. The gains obtained in [10] for the two-dimensional unsteady cases were indeed more modest than those for the steady cases but were worthwhile nevertheless, and we include here some results for three-dimensional unsteady cases at low and high Reynolds number for comparison.

The main application of the work described is the elucidation of the interaction of a stratified fluid with a three-dimensional obstacle. This can be complex and can lead to an extensive range of phenomena, such as lee-wave generation, wave breaking, and vortex shedding. To simulate wave breaking in particular requires the use not only of viscous equations but preferably of some kind of turbulence model. The turbulence model here is taken to be a simple mixing length model which merely allows the Reynolds number to be raised sufficiently for the phenomena to occur.

2. MATHEMATICAL MODEL

Equations of Motion

Here we are interested in the flow of a stably stratified fluid of finite depth D with buoyancy frequency N and free-stream velocity U past isolated three-dimensional obstacles of height h. This suffices as a simple model of atmospheric flow over arbitrary terrain, the behavior of which is characterized by the value of the dimensionless parameter $F_h = U/Nh$, the Froude number. Employing the Boussinesq approximation, in which density variations are neglected in the advection terms, the equations of motion describing unsteady turbulent stratified flow in Cartesian coordinates are

$$\frac{Du_i}{Dt} = -\frac{\partial \mathrm{p}}{\partial x_i} - \frac{1}{F_h^2}\theta\hat{z} + \frac{\partial}{\partial x_j}\left\{\frac{1}{\mathrm{Re}}\frac{\partial u_i}{\partial x_j} + \tau_{ij}\right\} \tag{1}$$

$$\frac{\partial u_j}{\partial x_j} = 0 \tag{2}$$

$$\frac{D\theta}{Dt} = \frac{\partial}{\partial x_j}\left\{\frac{1}{\mathrm{Re}\cdot\mathrm{Pr}}\frac{\partial \theta}{\partial x_j} + H_j\right\}. \tag{3}$$

Equation (1) represents conservation of momentum in each of the three coordinate directions, and (2) represents the continuity constraint. Equation (3) models the transport of the density scalar defined by $\theta = D(\rho - \rho_o)/h\Delta\rho$, where ρ is the physical density and $\Delta\rho$ is the magnitude of the density change over the nondimensional domain height D/h. $\hat{z}$ is the

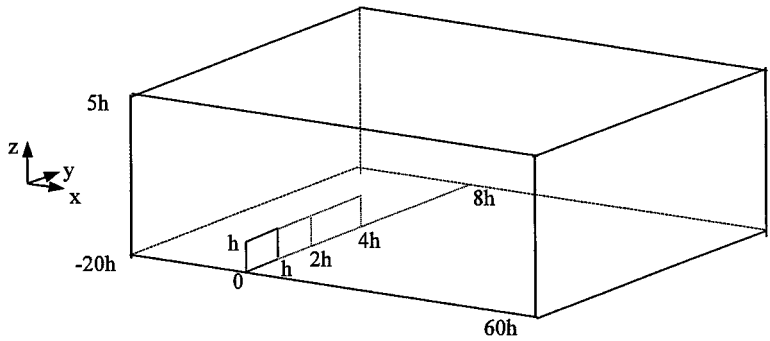

FIG. 1. Geometry of computational domain for three-dimensional flow past vertical barriers.

unit vector in the vertical direction. As in [10] the equations have been nondimensionalised by combinations of U, h, and ρ_o.

Although much of the work described here is for laminar flow we conclude the paper with a high Reynolds number flow, and for this reason we retain the Reynolds stress tensor τ_{ij} and turbulent bouyancy flux H_j terms which are absent in the laminar case. Pr is the turbulent Prandtl number, which is replaced by the Schmidt number Sc for laminar flows and is taken to be 1000.

Computational Domain and Boundary Conditions

The computational domain considered for the three-dimensional computations in this paper is illustrated in Fig. 1 and is somewhat akin to the experimental apparatus whereby an inverted obstacle is towed through a water tank; see [28], for example. The test problem for the Cartesian grid case is flow past a set of three vertical barriers of height h (taken to be unity) and increasing spanwise width of h, $2h$, and $4h$. The paper also includes results of computations over smooth obstacles, used for previous experimental [28] and numerical [29] studies, of cross-sectional shape given by $h(x) = 0.5[1 + \cos(\pi x/1.8)]$ with the ends formed by rotating the cross section through 180°. The aspect ratios of the obstacles (defined as the ratio of the distances between the spanwise and axial half-height points) are 1.0 (i.e., axisymmetric, COS1), 2.3 (COS2), and 3.7 (COS3). The grids in these cases are curvilinear and the algorithm employs a boundary-conforming transformation to stretch the vertical coordinate, which introduces volume scale factors and additional metric terms into the transport equations. Details of this are given in the Appendix.

In all cases symmetry conditions are applied in the centre plane ($y/h = 0$) and the bottom plane ($z/h = 0$). To be consistent with the experimental apparatus the boundary condition along the top plane ($z/h = D$) is a moving wall, although for the far side plane ($y/h = W$) this is relaxed to a symmetry condition. The boundary condition at inflow consists of uniform flow $(u, v, w) = (1, 0, 0)$ and a linear density variation for the stratified cases, while zero-derivative conditions are applied to all variables at outflow. The initial condition for all computations is uniform flow throughout the domain, and for the stratified cases a linearly varying density profile. In all the Cartesian cases $D = 5$ and $W = 8$. If W is taken to be 5 and the narrowest obstacle is chosen, then y and z are interchangable, and in this case the geometry is reduced to that considered by Hanazaki [30].

Scope of the Study

In flow of finite depth D the main parameter of interest is $K = ND/\pi U (K = D/\pi h F_h)$, the ratio of the velocity of the fastest internal wave mode to the free stream. Linear theory predicts that n (integer) sets of internal gravity waves will be present when $n < K \leq n + 1$. Accordingly, for $0 < K \leq 1$ (weak stratification) no lee waves occur since they are all swept downstream. For $K > 1$ (strong stratification) lee waves can occur, and one set is predicted when $1 < K \leq 2$ and so on. In the case of weak stratification, the suppression of vertical motion induced by the density gradient is manifested in the shortening of the separation length behind a bluff obstacle and an accompanying drag reduction. These qualitative features of the real turbulent flow, seen in laboratory experiments, can be reproduced in laminar computations with an appropriate value chosen for the Reynolds number, say $\mathrm{Re} = 50$ [28]. This was the value used for the earlier multigrid computations of steady two-dimensional stratified flows [10, 24] and is used for the corresponding three-dimensional flows described here.

While it is accepted that the flow is steady when $0 < K \leq 1$, for $K > 1$, however, wave propagation (upstream as well as downstream) means that the flow is unsteady and the time-dependent equations should be solved. In this paper we include results of the computation of unsteady flow over the set of vertical barriers at low Reynolds number ($\mathrm{Re} = 100$) and over the set of smooth obstacles at high Reynolds number ($\mathrm{Re} = 10^5$). The turbulence model used here is the extension of the mixing length model used in [10]. Although clearly lacking the sophistication of models using transport equations for turbulence quantities or better, it nevertheless enables high Reynolds number computations to be performed and is in fact the same kind of model used in many inviscid codes which simulate atmospheric flow—see [31], for example.

3. NUMERICAL METHOD

General

The discretization scheme used follows many of the standard practices of the finite volume method. Integrating the transport equations (1) and (3) over a typical control volume, of volume ΔV, the divergence theorem is applied to yield the usual discrete boundary integral

$$\sum \left[\left(u\varphi - \Gamma \frac{\partial \varphi}{\partial x} \right) \Delta A_{yz} + \left(v\varphi - \Gamma \frac{\partial \varphi}{\partial y} \right) \Delta A_{xz} + \left(w\varphi - \Gamma \frac{\partial \varphi}{\partial z} \right) \Delta A_{xy} \right] = S^{\varphi} \Delta V, \quad (4)$$

where φ is a typical variable. The summation is taken over the six faces of the control volume, and ΔA_{yz} denotes the area of the cell face in the y–z plane, etc. The grids are staggered according to the usual arrangement of variables and associated control volumes. Although this brings the usual geometrical complications, particularly in the three-dimensional case, no additional stabilizing terms need be added to the continuity equation, unlike the corresponding discretisation on collocated grids—see [32] for a recent review of the two approaches. The convective and diffusive contributions from the six cell faces are collected so that (4) can be expressed in the form

$$a_p \varphi_p = \sum a_m \varphi_m + S_p^{\varphi}, \quad (5)$$

where the summation is taken over the centres of the six neighbouring cells, and the multiplying coefficients contain the advective and diffusive flow rates. The source term includes the second-order corrections from the advective scheme (see later), the pressure gradient in the case of each momentum equation, and the buoyancy term in the case of the vertical momentum equation.

For unsteady flows the time derivative is approximated using the unconditionally stable second-order backward difference

$$\frac{3\varphi_p^{n+1} - 4\varphi_p^n + \varphi_p^{n-1}}{2\Delta t},$$

and inclusion merely amounts to minor changes to the diagonal coefficient and source term of Eq. (5).

The finest grid on which a solution is required is defined at the outset, and a hierarchy of grids is determined where the maximum numbers of lines on grid N_g ($N_g = 1$ corresponds to the finest grid) are IMAX_{N_g}, JMAX_{N_g}, and KMAX_{N_g}, in the x-, y-, and z-directions, respectively. Efficient use of storage space is important in three-dimensional simulations and all variables are stored in single-dimensional arrays which follow rows in the x-direction, so that consecutive elements contain variables which are neighbours upstream and downstream in general. The element at position $(I,\ J,\ K)$ on grid N_g is addressed using a pointer system of the form

$$M = I + (J-1) \times \mathrm{IMAX}_{N_g} + (K-1) \times \mathrm{IMAX}_{N_g} \times \mathrm{JMAX}_{N_g} + \mathrm{NG}_{N_g},$$

where NG_{N_g} is a summation term over the grids defined by

$$\mathrm{NG}_1 = 0, \qquad \mathrm{NG}_{N_g} = \mathrm{NG}_{N_{g-1}} + \mathrm{IMAX}_{N_{g-1}} \times \mathrm{JMAX}_{N_{g-1}} \times \mathrm{KMAX}_{N_{g-1}}, \qquad \mathrm{N}_g > 1.$$

Although the method has been implemented only on serial machines, there is no reason in principle why it should not run on a parallel machine, or a networked cluster of pcs, for example. Work is under way with a Java-based version of the code to evaluate this latter approach.

Smoothing Algorithm

Supposing that the discrete steady momentum equations are satisfied by u, v, w, p, and θ, Eq. (5) takes the form for the six velocities associated with a continuity control volume as

$$a^u_{i-1/2jk} u_{i-1/2jk} = \sum a^u_m u_m + A^u_{i-1/2jk}(p_{i-1jk} - p_{ijk}) + S^u_{i-1/2jk} \tag{6}$$

$$a^u_{i+1/2jk} u_{i+1/2jk} = \sum a^u_m u_m + A^u_{i+1/2jk}(p_{ijk} - p_{i+1jk}) + S^u_{i+1/2jk} \tag{7}$$

$$a^v_{ij-1/2k} v_{ij-1/2k} = \sum a^v_m v_m + A^v_{ij-1/2k}(p_{ij-1k} - p_{ijk}) + S^v_{ij-1/2k} \tag{8}$$

$$a^v_{ij+1/2k} v_{ij+1/2k} = \sum a^v_m v_m + A^v_{ij+1/2k}(p_{ijk} - p_{ij+1k}) + S^v_{ij+1/2k} \tag{9}$$

$$a^w_{ijk-1/2} w_{ijk-1/2} = \sum a^w_m w_m + A^w_{ijk-1/2}(p_{ijk-1} - p_{ijk}) + S^w_{ijk-1/2} \tag{10}$$

$$a^w_{ijk+1/2} w_{ijk+1/2} = \sum a^w_m w_m + A^w_{ijk+1/2}(p_{ijk} - p_{ijk+1}) + S^w_{ijk+1/2} \tag{11}$$

where

$$A^u_{i-1/2jk} = \frac{\Delta A^u_{i-1/2jk}}{\Delta x^u_{i-1/2jk}}, \quad \text{etc.}$$

The source terms have been multiplied by the volumes of respective control volumes and the pressure gradient is shown explicitly. The discrete continuity equation is

$$\begin{aligned}&\left(u_{i+1/2jk} - u_{i-1/2jk}\right)\Delta A^x_{ijk} \\ &\quad + \left(v_{ij+1/2k} - v_{ij-1/2k}\right)\Delta A^y_{ijk} + \left(w_{ijk+1/2} - w_{ijk-1/2}\right)\Delta A^z_{ijk} = 0. \end{aligned} \tag{12}$$

For stratified flow the density transport equation takes the form

$$a^\theta_{ijk}\theta_{ijk} = \sum a^\theta_m \theta_m + S^\theta_{ijk}, \tag{13}$$

while the sources in the vertical momentum equation are modified to include the discrete bouyancy term

$$\frac{\Delta A^w_{ijk-1/2}}{2F_h^2}(\theta_{ijk-1} + \theta_{ijk}).$$

Decoupled Smoother (SIMPLE)

The SIMPLE pressure correction algorithm [5] is well known. The coefficients in each of the discrete momentum equations (6)–(11) are calculated over the whole domain and using the current pressure field the equations are solved globally in turn via an ADI sweep to yield an updated velocity field. Coupling is then obtained between the local velocities and pressures using relations derived from the discrete momentum equations. These are substituted into the discrete continuity equation (12) (written terms of velocity corrections) to derive a Poisson-type equation for the pressure corrections. The pressure correction equation is solved (here using four ADI sweeps) to yield the pressure corrections, which are used to update the pressure and the velocities. In the case of stratified flow the density transport equation (13) is solved prior to the iteration being repeated.

Discretisation of Advective Term

The treatment of the advective terms is based on the assumption that the flow across cell boundaries is one-dimensional in directions normal to the cell faces. Denoting the values of the flow variable at the centres of consecutive cells by φ_{i-1}, φ_i, and φ_{i+1}, many schemes exist to provide an estimate at the downwind cell face, $\varphi_{i+1/2}$. The general form of the κ-scheme [33] provides a convenient representation,

$$\varphi_{i+1/2} = \frac{1}{2}(\varphi_i + \varphi_{i+1}) + \frac{1-\kappa}{4}(-\varphi_{i-1} + 2\varphi_i - \varphi_{i+1}),$$

where several schemes are encompassed as κ ranges from $\kappa = -1$ (second-order upwind) to $\kappa = 1$ (central differencing). Monotonicity properties can be introduced by defining the normalised variable [34]

$$\tilde{\varphi} = \frac{\varphi - \varphi_{i-1}}{\varphi_{i+1} - \varphi_{i-1}}.$$

The monotonicity condition is that $\tilde{\varphi}_i \le \tilde{\varphi}_{i+1/2} \le 1$ whenever $0 \le \tilde{\varphi}_i \le 1$, and it is well known that the κ-scheme as it stands fails to fulfill this for any value of κ. The scheme may be made nonlinear, so that

$$\tilde{\varphi}_{i+1/2} = f(\tilde{\varphi}_i),$$

where f is a limiter function introduced to ensure monotonicity, for example, the cubic polynomials defined by Wesseling *et al.* [35].

These ideas are entirely parallel to the TVD [36] framework, where the corresponding formulation is

$$\varphi_{i+1/2} = \varphi_i + \frac{1}{2}\Psi(R)(\varphi_i - \varphi_{i-1}),$$

where R is the ratio of the successive slopes

$$R = \frac{\varphi_{i+1} - \varphi_i}{\varphi_i - \varphi_{i-1}}$$

and Ψ is a limiter function. Since R and the normalised variable $\tilde{\varphi}_i$ are related through $R + 1 = 1/\tilde{\varphi}_i$ the TVD scheme can be written in terms of normalised variables as

$$\tilde{\varphi}_{i+1/2} = \tilde{\varphi}_i \left(1 + \frac{1}{2}\Psi\right).$$

Thus for any limiter function Ψ there is a function f, so that the harmonic limiter [37]

$$\Psi(R) = (|R| + R)/(R + 1)$$

is equivalent to the function $f(\tilde{\varphi}_i) = \tilde{\varphi}_i(2 - \tilde{\varphi}_i)$, while the van Albada limiter [38]

$$\Psi(R) = (R^2 + R)/(R^2 + 1)$$

is equivalent to $f(\tilde{\varphi}_i) = (4\tilde{\varphi}_i^3 - 5\tilde{\varphi}_i^2 + 3\tilde{\varphi}_i)/(4\tilde{\varphi}_i^2 - 4\tilde{\varphi}_i + 2)$. The TVD region and these limiter functions are illustrated in the normalised variable diagram in Fig. 2, along with the

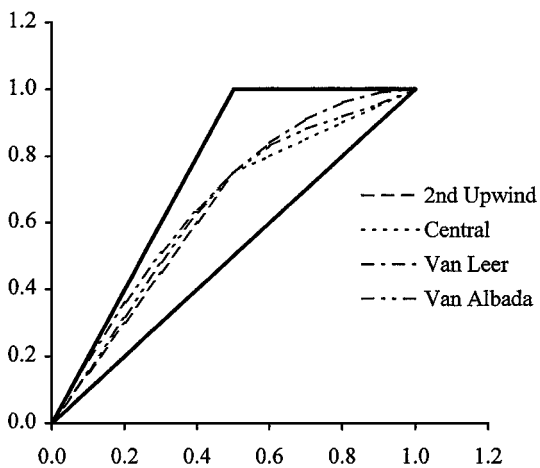

FIG. 2. Monotonic region for advective schemes.

piecewise linear function corresponding to the combination of second-order upwinding and central differencing given by

$$f(\tilde{\varphi}_i) = \begin{cases} 3\tilde{\varphi}_i/2 & \text{when } 0 \le \tilde{\varphi}_i \le 1/2, \\ (\tilde{\varphi}_i + 1)/2 & \text{when } 1/2 < \tilde{\varphi}_i \le 1. \end{cases}$$

It has been shown previously [17] that the particular type of limiter can affect the convergence rate of a multigrid iteration, and similar behavior is found here. Although complex to analyse in any detail, it can be seen from the form of the coarse grid equation for nonlinear operators that difficulties might be anticipated. For any of the transported variables the general coarse grid equation (the counterpart to (5)) can be expressed as

$$a_{2h}\varphi_{2h} - \sum a_{2h}\varphi_{2h} = S^{\varphi}_{2h} + \left\{ a_{2h}\tilde{\varphi}_{2h} - \sum a_{2h}\tilde{\varphi}_{2h} - S^{\tilde{\varphi}}_{2h} \right\} + I^{2h}_{h} R^{\varphi}_{h}. \qquad (14)$$

The first term on the right-hand side is the source term for the current coarse grid approximation φ_{2h}, the term in curly brackets is evaluated from the restricted solution $\tilde{\varphi}_{2h}$, while the last term represents the restricted fine grid residuals. In addition to the pressure gradient and bouyancy term in the case of the momentum equations, the source terms S^{φ}_{2h} and $S^{\tilde{\varphi}}_{2h}$ contain the high-order part of the convective discretisation and when flux limiters are implemented these are the nonlinear functions outlined above. If the coefficients in (14) are held fixed, then we have

$$a_{2h}\varphi'_{2h} - \sum a_{2h}\varphi'_{2h} = S^{\varphi}_{2h} - S^{\tilde{\varphi}}_{2h} + I^{2h}_{h} R^{\varphi}_{h},$$

where $\varphi'_{2h} = \varphi_{2h} - \tilde{\varphi}_{2h}$. When the source terms are linear functions of the discrete variables, convergence of the fine grid residuals implies that the coarse grid iteration will result in convergence to zero of the coarse grid corrections; i.e., $R^{\varphi}_{h} \to 0$ implies $\varphi'_{2h} \to 0$. However, when the source terms are nonlinear functions of the discrete variables, this need no longer be the case, and the guarantee of convergence would appear to be lost. This is certainly consistent with some of the numerical experiments described later, when convergence difficulties are found with the harmonic and van Albada limiters but convergence is restored with the use of the piecewise linear limiter.

Underrelaxation

Underrelaxation is vital for convergent iteration. Typical values of the underrelaxation factors for the momentum equations for neutral flow are similar in three dimensions to those used in two, say 0.7. The pressure correction equation itself is not underrelaxed, but only a fraction, say 0.5, of the resulting pressure corrections is added to the current pressure field.

For stratified flow a grid-dependent strategy was adopted. The underrelaxation factors required to solve the coarse grid transport equations on the coarsest grid were found to be smaller than those for all other grids, where the iteration only smoothes the solution, and the factors required for the w-momentum and the density equations were smallest of all. However, it was found that increasing the fraction of the pressure changes added, even to unity, improved the rate of convergence as stratification increased. Clearly there is no

TABLE I
Underrelaxation Factors for Steady Computations

F_h/K	U_{mom}	V_{mom}	W_{mom}	Pressure	Density
∞/0.0	0.7	0.7	0.7	0.5	—
	0.7	0.7	0.7	0.5	—
3.180/0.5	0.7	0.7	0.7	0.7	0.9
	0.6	0.6	0.4	0.7	0.4
1.989/0.8	0.6	0.6	0.6	1.0	0.6
	0.4	0.4	0.2	1.0	0.2
1.592/1.0	0.4	0.4	0.4	1.0	0.4
	0.4	0.4	0.2	1.0	0.2
1.224/1.3	0.3	0.3	0.3	1.0	0.3
	0.3	0.3	0.15	1.0	0.2

Note. The lower line in each case applies to the coarsest grid, the upper line to all other grids.

theoretical guidance here, and optimal strategies are found by trial and error. Typical values used are given in Table I.

Multigrid Implementation

The multigrid implementation follows standard procedures outlined in many places—see [23] for general discussion and [10, 27] for discussion specific to the applications described here. Restriction of flow variables is carried out using means of nearest neighbors, weighted according to cell areas in the case of the velocities to preserve mass fluxes. For non-Cartesian grids the procedure requires modification taking into account the coordinate transformation—see [10] for one approach. Restriction of residuals is by summation to preserve integrals, with all residuals reevaluated prior to restriction. Prolongation is by trilinear interpolation, with care taken around the vertical barrier when present. The cycling algorithm uses W cycles with up to four grid levels with one pre- and one post-smoothing iteration on each, except the coarsest where the equations are solved with 10 iterations.

Multigrid convergence rates are dependent on the extent of ellipticity in the discrete equations and this decreases as diffusive parameters increase. The density equation here has a smaller diffusive parameter than the momentum equations, and this equation may be solved a number of times (typically three times)—corresponding to increasing the number of pre- and post-smoothing iterations. This avoids the convergence of the whole multigrid process being excessively delayed by one otherwise slowly converging component.

4. RESULTS AND DISCUSSION

Steady Two-Dimensional Flow

We describe the results of computations performed with various limiter functions for low Reynolds number ($\text{Re} = 50$) flow over the two-dimensional vertical barrier described in [10]. The same grid arrangements are used as in that study, with the finest grid comprising

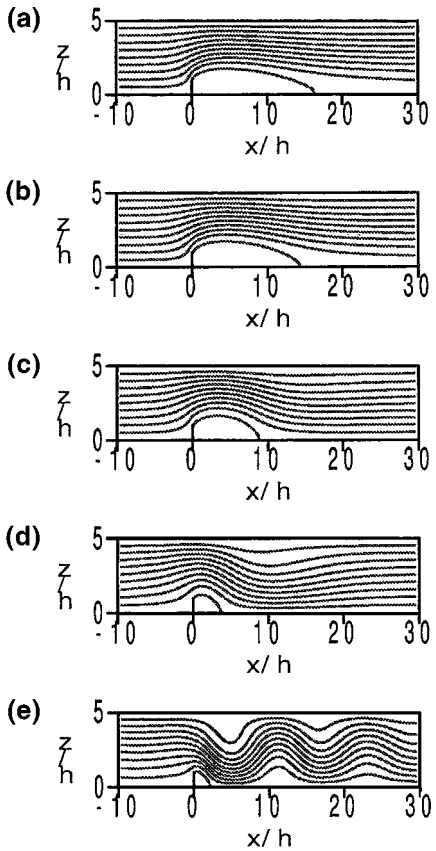

FIG. 3. Streamlines for flow over two-dimensional vertical barrier with (a) $F_h = \infty$, $K = 0$ (neutral flow), (b) $F_h = 3.180$, $K = 0.5$, (c) $F_h = 1.989$, $K = 0.8$, (d) $F_h = 1.592$, $K = 1.0$, and (e) $F_h = 1.224$, $K = 1.3$.

320×80 continuity control volumes, enabling 5 grid levels to be defined with the coarsest containing 20×5 continuity control volumes. The grids employ nonuniform spacing and the minimum grid spacing in each direction (at the barrier tip) is 0.1 h. Streamline plots for the five cases (a) $F_h = \infty$, $K = 0$ (neutral flow), (b) $F_h = 3.180$, $K = 0.5$, (c) $F_h = 1.989$, $K = 0.8$, (d) $F_h = 1.592$, $K = 1.0$, and (e) $F_h = 1.224$, $K = 1.3$ are shown in Fig. 3. These plots demonstrate the characteristic shortening of the recirculation zone for $K \leq 1$ and the appearance of downstream lee waves for $K > 1$.

For the neutral case the second-order schemes converged largely in unison to a certain tolerance level, and although differences in asymptotic rate occurred thereafter, all schemes produced acceptable results. The limited schemes converged somewhat more slowly than the second-order upwind scheme, with the piecewise linear scheme performing the least well. The asymptotic rate of the second-order upwind scheme was at least as good as the first-order upwind scheme. The convergence of the separation length with respect to grid refinement is illustrated in Fig. 4, where this quantity is plotted against the square of the grid spacing at the barrier tip. Only the second-order upwind scheme gave a fully convincing demonstration of second-order accuracy, while the limited schemes produce results which are close to each other, but appear to be contaminated with some first-order behavior, shown to its fullest extent by the first-order scheme. Degradation of accuracy of high-order nonlinear schemes is known to occur downstream of captured shock waves in

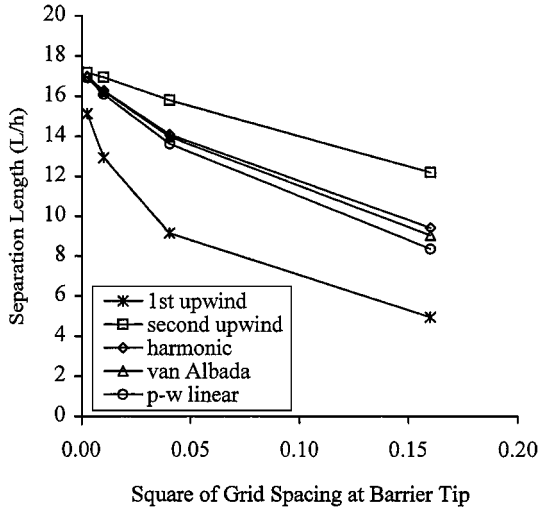

FIG. 4. Variation of separation length with grid refinement for various advection schemes.

multidimensional flows [40, 41], although in the smooth regions of the flow design order of accuracy is still achieved, contrasting with the results presented here.

Consider next the case with $F_h = 3.180$, $K = 0.5$ shown in Fig. 3b. While superficially only little different from the neutral case, the presence of the density transport equation, which is strongly dominated by convection when $\mathrm{Sc} = 1000$, has a major impact on the asymptotic convergence rate. Computations were performed with the harmonic limiter for the momentum equations and five different schemes applied to the density transport equation. The only combination to produce good asymptotic convergence was that with the first-order upwind scheme on the density equation. In this case, high levels of diffusion spuriously boost the ellipticity in the discretisation. This occurs to a much lesser extent for the second-order schemes resulting in slowed convergence. Smoothing rates can generally be improved, however, by increasing the number of pre- and post-smoothing iterations. Experiments with the piecewise linear scheme on the density equation and an increasing number of pre- and post-smoothing iterations demonstrated greatly improved convergence rates. Of course, the additional iterations increase the expense of the computation, and in terms of computing time three pre- and post-smoothing iterations were found to be optimal. However, not all the limiters applied to the density equation responded in this way, and in fact the piecewise linear limiter was the only one of the three to do so, as illustrated in Fig. 5, where the usual definition of the residual norm

$$R = \left[\frac{\sum (R^u)^2 + \sum (R^w)^2 + \sum (R^c)^2 + \sum (R^\theta)^2}{4 \times \mathrm{IMAX}_{N_g} \times \mathrm{KMAX}_{N_g}} \right]^{1/2},$$

is plotted after each multigrid cycle. The convergence histories of computations with all the limited schemes demonstrate the poor convergence properties of the harmonic and van Albada limiters when applied to the density equation. Although further work is required to fully understand the nature of the failure to converge, this is currently attributed to the nonlinearity of the limiter functions undermining the convergence of the multigrid process as outlined earlier.

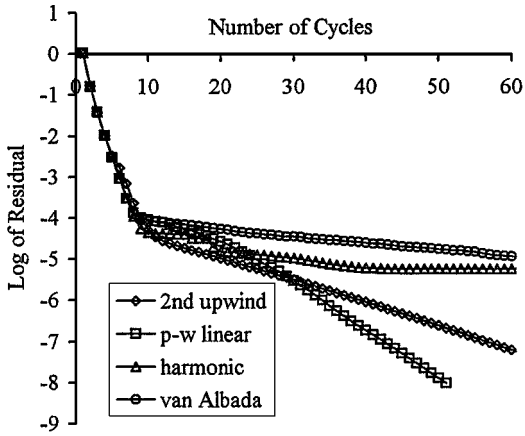

FIG. 5. Convergence histories for various schemes applied to the density equation with three pre- and post-smoothing iterations ($F_h = 3.180$, $K = 0.5$).

With the convergence characteristics thus improved from the work in [10, 24] the algorithm was used to compute the other stratified cases shown in Fig. 3. The case with $F_h = 1.224$, $K = 1.3$ (Fig. 3e) is difficult to compute, partly because of the upstream disturbance and partly because the flow field in any case does not appear to be steady. Previous attempts with the harmonic limiter on the density equation produced only a divergent iteration, although with the piecewise linear limiter a slowly convergent iteration can be achieved. However, it was found for this case that the use of the harmonic limiter on the velocities did not achieve a convergent iteration on all the grids attempted, but the use of the piecewise linear limiter on all variables did. The convergence difficulties for this case compared with the others are illustrated in Fig. 6, where the histories for all these computations on a 160×40 grid are shown.

Steady Neutral Three-Dimensional Flow

Prior to the description of the corresponding three-dimensional stratified cases we turn now to the computation of three-dimensional neutral flow at the same Reynolds number,

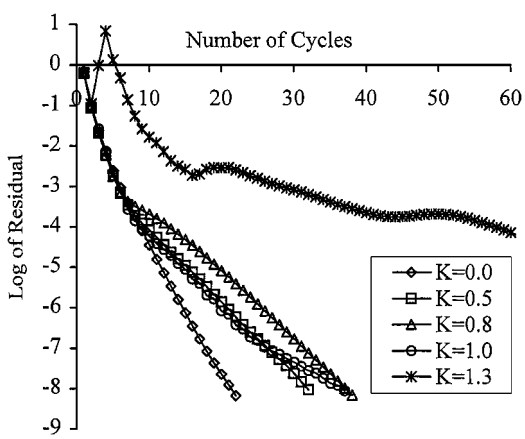

FIG. 6. Variation in convergence rate with increasing density stratification for two-dimensional flow.

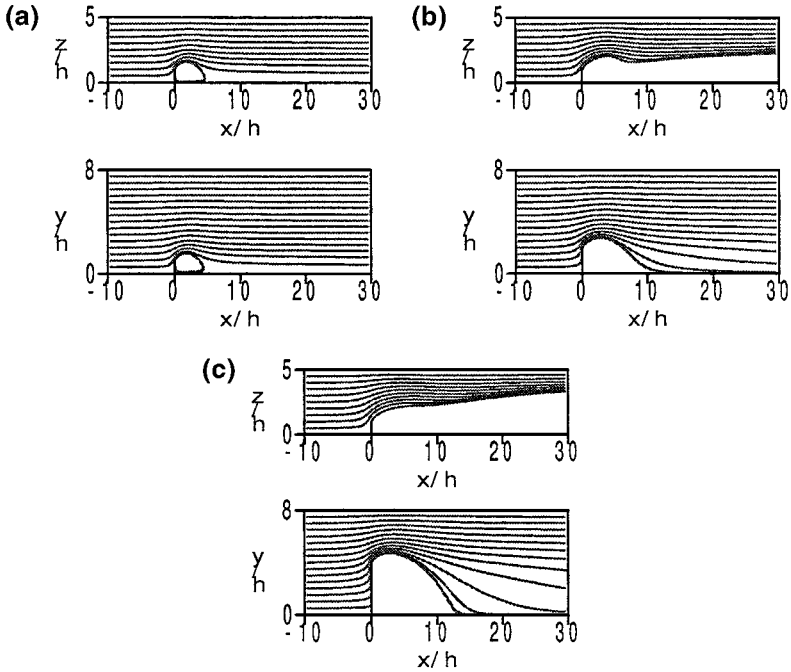

FIG. 7. Streamlines for neutral flow past three-dimensional obstacles with (a) $w/h = 1$, (b) $w/h = 2$, and (c) $w/h = 4$.

$\mathrm{Re} = 50$. The grid spacings in the x- and z-directions for the three-dimensional computations correspond to those of the two-dimensional grid containing 160×40 cells, while the spacings in the y-direction are similar to those in the z-direction. The finest grid used here thus contains $160 \times 40 \times 40$ cells from which three other grids are defined containing $80 \times 20 \times 20$, $40 \times 10 \times 10$, and $20 \times 5 \times 5$ cells. Multigrid computations have been performed with the harmonic limiter on grids of sizes $40 \times 10 \times 10$, $80 \times 20 \times 20$, and $160 \times 40 \times 40$ permitting two, three, and four grid levels, respectively.

Streamlines originating upstream in the centre plane ($y/h = 0$) and the bottom plane ($z/h = 0$) are shown in Fig. 7 for computations on the finest grid and should be compared with Fig. 3a for the corresponding flow over the infinite width obstacle. As anticipated from the geometry, the wake flow for the narrowest barrier is virtually y–z symmetric, while for the two wider obstacles it clearly is not. Spanwise recirculation dominates in these cases, displacing the flow in the centre plane vertically upwards. Examination of the separation lengths and the drag values for these flows shows that both quantities increase with barrier width as expected, with the convergence behavior being achieved similar to that observed in the two-dimensional case.

The performance of the decoupled algorithm SIMPLE is summarised in Table II, which gives the number of multigrid cycles and computing times required to achieve a converged solution of the flow past each obstacle on the three grids, as well as the corresponding two-dimensional case. Convergence here is monitored using sums of absolute values of residuals over the entire domain and a computation is deemed to have converged when the maximum sum over the four equations falls below 10^{-4}. The computing times given are for double precision arithmetic on a Silicon Graphics Indigo workstation. It is seen that the timings for the three-dimensional computations are approximately those anticipated by extrapolation

TABLE II
Numbers of Multigrid Cycles and Computing Times with the SIMPLE Method for Neutral Flow, $F_h = \infty$, $K = 0.0$

Aspect ratio/grid	$40 \times 10 \times 10$	$80 \times 20 \times 20$	$160 \times 40 \times 40$
1	14 (31.0 s)	13 (3 m 16 s)	11 (26 m 16 s)
2	18 (39.2 s)	15 (3 m 58 s)	13 (31 m 3 s)
4	18 (39.2 s)	18 (4 m 51 s)	16 (38 m 12 s)
∞ ($2D$)	19 (1.9 s)	14 (5.0 s)	13 (18.5 s)

from the two-dimensional results (multiplication by $9/4$ times the number of spanwise grid planes). The results for the computation on each grid indicate only minor variation with obstacle width, and for each obstacle the number of cycles exhibits a good degree of grid independence (the number of cycles actually reduces slightly with grid refinement). The consequence is that computing times increase by a factor of approximately 8 when the number of cells is doubled in each direction. As an indication of the amount of work being saved the computation for the narrowest obstacle on the finest grid took around 25 times as long to achieve the same level of convergence—the factor for the wider obstacles is likely to be greater. This compares with speedup factors of around 9 for the computation of the corresponding two-dimensional flow on the 160×40 grid and 29 on the 320×80 grid [10]. Asymptotic convergence rates for the decoupled algorithm are shown in Fig. 8. Shown for comparison is the convergence rate of the corresponding computation on a 160×40 grid, from which it is clear that the asymptotic rates deteriorate significantly with the addition of the third dimension. This contrasts with the behavior for the two- and three-dimensional driven cavities [27], where the asymptotic rates were very similar for all Reynolds numbers tried (up to 1000).

Steady Stratified Three-Dimensional Flow

Computations of three-dimensional stratified flow have been performed for the three obstacles for the same values of the stratification as for the two-dimensional cases discussed

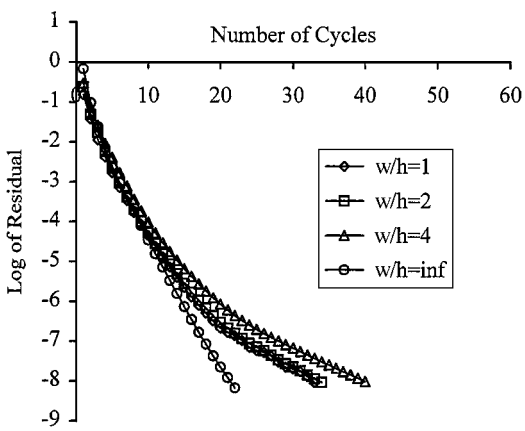

FIG. 8. Convergence histories for neutral flow past obstacles with the SIMPLE smoother.

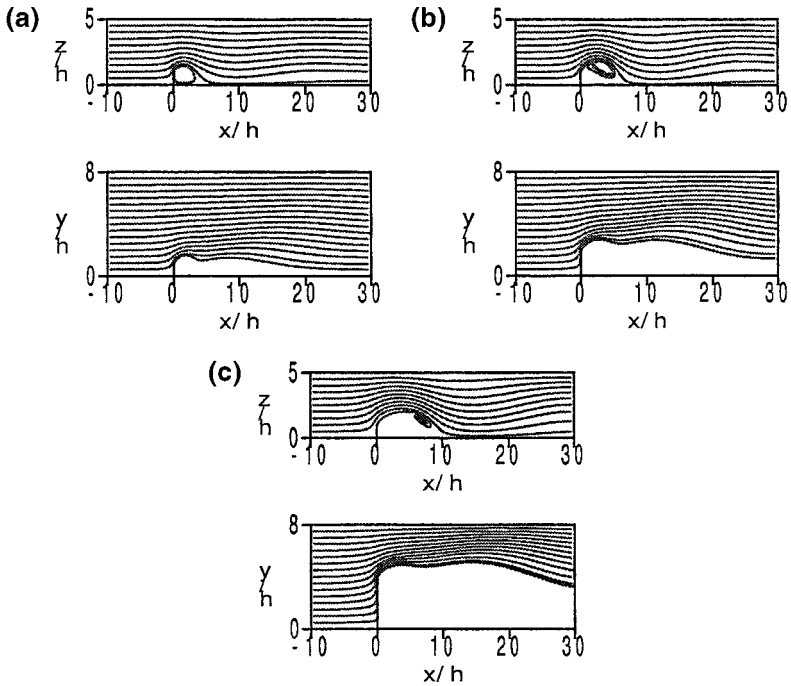

FIG. 9. Streamlines for stratified flow ($F_h = 3.180$, $K = 0.5$) past three-dimensional obstacles with (a) $w/h = 1$, (b) $w/h = 2$, and (c) $w/h = 4$.

earlier, namely $F_h = 3.180\,(K = 0.5)$, $F_h = 1.989\,(K = 0.8)$, $F_h = 1.592\,(K = 1.0)$, and $F_h = 1.224\ (K = 1.3)$. In each case the piecewise linear limiter was used for the density equation, with three pre- and post-smoothing iterations. Unlike the two-dimensional stratified cases, the underrelaxation factors now had to be dependent on both the grid and the level of stratification as described above and in Table I. Streamline plots for $F_h = 3.180\,(K = 0.5)$ and $F_h = 1.224\,(K = 1.3)$ are shown in Figs. 9 and 10, respectively, to be compared with the corresponding two-dimensional cases in Fig. 3, and the multigrid performances are given in Tables III and IV.

The effects of the stratification on the wake flow compared with the neutral case increase with obstacle width, as seen in the streamline plots in Fig. 9. The reaction to the vertical restoring force in the x–z plane appears to be minimal for the narrowest barrier, while for the widest it produces dramatic change. For all three obstacles, however, there is clear evidence of streamline overshoot, which is quite absent for the corresponding two-dimensional case (Fig. 3b). The streamlines in the x–y plane also demonstrate profound differences from the neutral case (Fig. 7), for the downward force now competes with spanwise recirculation as the major influence determining the wake flow.

The general effects of the stratification are more pronounced for $F_h = 1.989$, $K = 0.8$. Although linear theory predicts no lee waves while $K < 1$, and they do not occur in the two-dimensional case (Fig. 3c), wave structures are apparent for each of the three-dimensional cases (also noted in [30]), with the amplitude increasing with increasing obstacle width. The case $F_h = 1.592\,(K = 1.0)$ shows further evidence of lee waves, with still none in the two-dimensional case (Fig. 3d). Lee waves occur for all obstacles at $F_h = 1.224\,(K = 1.3)$ (Fig. 10), where the trends of increasing amplitude with obstacle width, as well as increasing wavelength, are observed.

TABLE III
Numbers of Multigrid Cycles and Computing Times for Stratified Flow, $F_h = 3.182$, $K = 0.5$

Aspect ratio/grid	$40 \times 10 \times 10$	$80 \times 20 \times 20$	$160 \times 40 \times 40$
1	15 (1 m 1 s)	14 (5 m 39 s)	16 (66 m 40 s)
2	19 (1 m 12 s)	16 (6 m 32 s)	16 (66 m 40 s)
4	22 (1 m 20 s)	21 (8 m 34 s)	19 (79 m 10 s)
∞ ($2D$)	16 (3.0 s)	15 (11.7 s)	17 (46.0 s)

TABLE IV
Numbers of Multigrid Cycles and Computing Times for Stratified Flow, $F_h = 1.224$, $K = 1.3$

Aspect ratio/grid	$40 \times 10 \times 10$	$80 \times 20 \times 20$	$160 \times 40 \times 40$
1	40 (2 m 32 s)	43 (17 m 32 s)	65 (273 m 10 s)
2	47 (2 m 49 s)	53 (21 m 43 s)	69 (289 m 51 s)
4	55 (3 m 23 s)	65 (27 m 07 s)	81 (340 m 23 s)
∞ ($2D$)	35 (6.4 s)	30 (21.4)	73 (3 m 17 s)

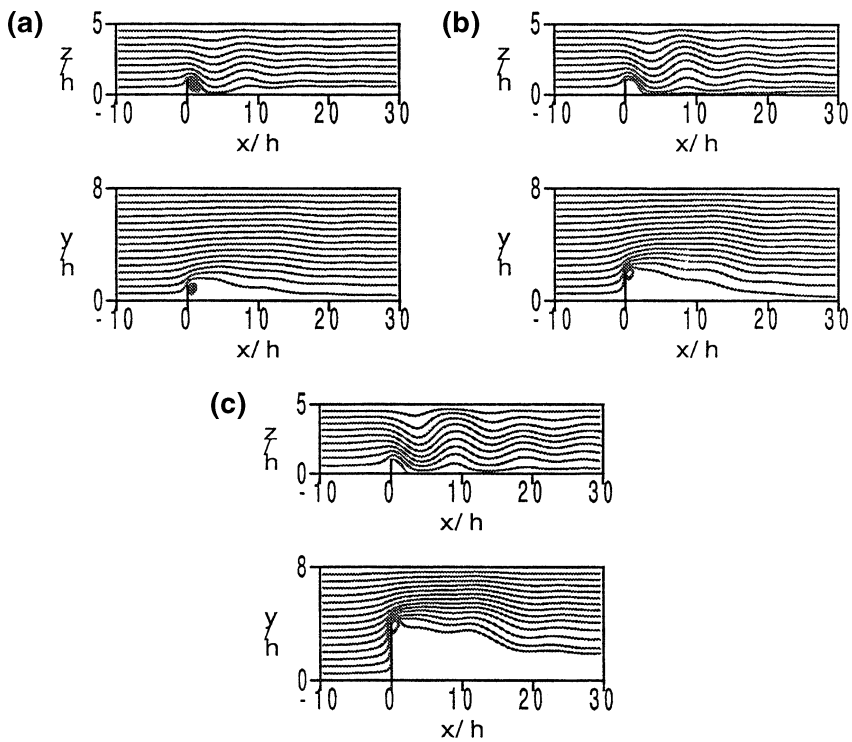

FIG. 10. Streamlines for stratified flow ($F_h = 1.224$, $K = 1.3$) past three-dimensional obstacles with (a) $w/h = 1$, (b) $w/h = 2$, (c) $w/h = 4$.

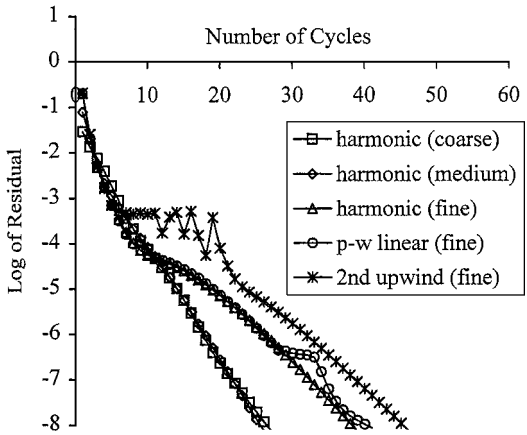

FIG. 11. Convergence histories for stratified flow ($F_h = 3.180$, $K = 0.5$) past the narrowest obstacle.

The convergence data in Tables III and IV show that the time per cycle has increased by approximately 70% in comparison with the neutral case, accounted for by the additional work of solving the density equation three times. In fact this could be reduced, for it is only the nonlinear source terms which need be reevaluated, not the entire set of left-hand-side coefficients as currently implemented. The number of multigrid cycles required to achieve convergence is always greater than that for the neutral case, as expected, and as in the neutral case this number increases with obstacle width for each value of the Froude number tried. The number of cycles required also increases with the level of stratification, although for $K = 0.5$ and $K = 0.8$ this is largely grid independent. For $K = 1.0$ and $K = 1.3$, on the other hand, the number of cycles rises with grid refinement, so that the total amount of work required on the finest grid for the widest obstacle with $K = 1.3$ is approximately four times that required for the narrowest obstacle with $K = 0.5$.

Figure 11 shows the convergence histories with grid refinement for the first stratified case, $F_h = 3.180$, $K = 0.5$, for the narrowest obstacle. In this instance all three schemes used for the momentum equations produced convergent iterations. However, as noted previously for one of the two-dimensional cases, it was also found here that the limiter used for the velocities could influence whether or not a particular case converged. Although the piecewise linear limiter generally proved more robust than the harmonic, it did not always produce asymptotic convergence, and the second-order upwind scheme had to be used instead. For the case $F_h = 1.989$, $K = 0.8$, for example, the piecewise linear limiter leads to a convergent iteration for the wider obstacles, but not the narrowest. As in the two-dimensional computations, the asymptotic convergence rates fall with increasing stratification, and Fig. 12 demonstrates this for each of the five computations of flow past the narrowest obstacle. The general deterioration in convergence rates compared with the two-dimensional cases is clear from comparison with Fig. 6.

The variation in pressure drag and separation length for each of the four barriers has been analysed. In all cases both quantities fall as K increases from zero to unity, consistent with previous observations [10, 28, 30]. Although it was noted that wave structures are present when $K = 0.8$ for the three-dimensional flows, the drag continues to fall for this value, and the expected sharp increase in drag associated with the production of lee waves does not actually occur until $K > 1$. The separation length, on the other hand, does continue to

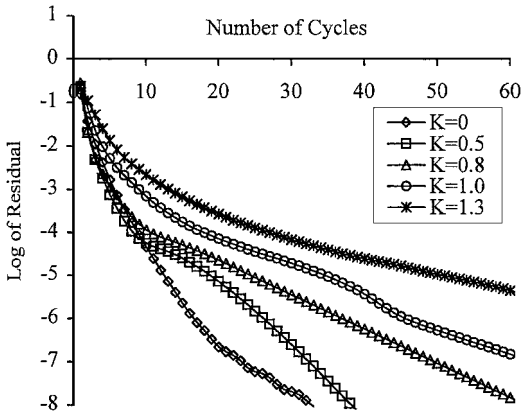

FIG. 12. Variation in convergence rate with increasing density stratification for three-dimensional flow.

fall and for both quantities the effects generally increase with obstacle width. The lee-wave wavelengths for the two-dimensional flows have been found previously to follow the finite depth limit, $\lambda = 2D/(K^2 - 1)^{1/2}$, while those appearing in the three-dimensional flows are shorter, with the wavelength shortening with obstacle width, so that the lee waves produced by the narrowest obstacle are much closer to the infinite depth limit, $\lambda = 2\pi h F_h = 2D/K$.

Unsteady Stratified Three-Dimensional Flow

Having demonstrated the capability of convergent multigrid iteration for steady three-dimensional stratified flows, we turn finally to time-dependent cases. The time-stepping is achieved via the second-order backward formula given earlier and tests confirm that the present algorithm converges in a second-order manner in time. Some indication of the benefit of using multigrid for unsteady computations was given in [10] for two-dimensional flows, where computations of unsteady flow over the vertical barrier were performed at low Reynolds number and with a mixing length turbulence model at high Reynolds number. Modest gains were demonstrated, which increased with the size of time step, and here we extend the study to include three-dimensional unsteady cases and present two sets of results for comparison.

The first is for laminar flow (Re $= 100$) past the set of three-dimensional vertical barriers in a channel of height $D/h = 5$ already described, for which $F_h = 1.061$, $K = 1.5$. This case demonstrates the periodic unsteadiness found in laboratory experiments [28] and numerical simulations [30, 42] and subsequently explained in terms of a wave mode with stationary group velocity [43]. To allow for wave propagation upstream and downstream the grid was extended to cover $-100 \le x/h \le 100$ and the grid sizes used increased to $50 \times 10 \times 10$, $100 \times 20 \times 20$, and $200 \times 40 \times 40$. According to estimates based on linear theory this enables computation up to a nondimensional time of $Ut/h = 240$ before wave reflections are due back at the barrier. As in [10] computations are performed up to $Ut/h = 200$ with each of the three barriers on each of the three grids and with two time steps, $U\Delta t/h = 2.0$ and $U\Delta t/h = 1.0$. There is now no need to obtain an asymptotically converged solution at each time step and for all cases the convergence criterion before advancing to the next is that the maximum sum of the absolute values of residuals over each of the five equations reaches 5×10^{-4}. (An additional consequence of practical benefit is that the computations can now be adequately performed in single precision arithmetic.)

TABLE V

Numbers of Multigrid Cycles, Computing Times, and Speedup Factors for Unsteady Stratified Flow past Widest Barrier, F_h = 1.061, K = 1.5, and Re = 100

$U\Delta t/h$	$50 \times 10 \times 10$	$100 \times 20 \times 20$	$200 \times 40 \times 40$
2.0	5 (11.9 s, 1.5)	6 (2 m 7 s, 3.4)	7 (21m 45 s, 6.7)
1.0	4 (8.8 s, 1.5)	5 (1 m 46 s, 2.4)	5 (16 m 15 s, 5.2)

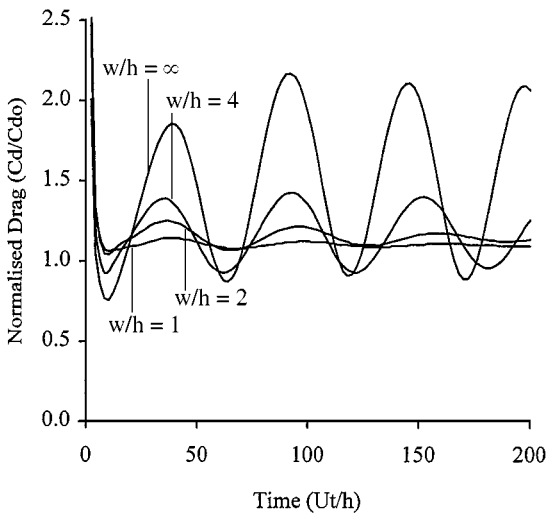

FIG. 13. Variation in normalised drag for unsteady flow past the two-dimensional and the three three-dimensional barriers with $F_h = 1.062$, $K = 1.5$, and Re $= 100$.

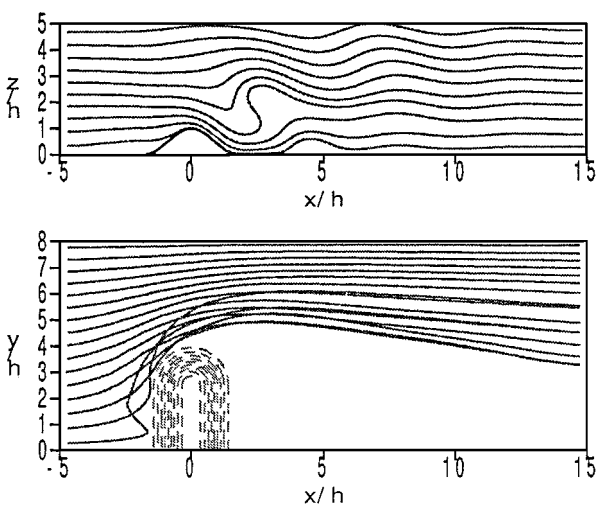

FIG. 14. Instantaneous streamlines at $Ut/h = 20$ for unsteady flow past the widest three-dimensional cosine-shaped obstacle ($w/h = 3.7$) with $F_h = 0.7$, $K = 4.55$, and Re $= 100{,}000$.

TABLE VI

Numbers of Multigrid Cycles, Computing Times, and Speedup Factors for Unsteady Stratified Flow past Cosine-Shaped Obstacles, $F_h = 0.7$, $K = 4.55$, and Re = 100,000

$U\Delta t/h$	COS1	COS2	COS3
1.0	7 (43 m, 3.3)	8 (49 m, 5.3)	10 (61 m, 5.8)
0.5	4 (24 m, 1.8)	5 (30 m, 2.1)	5 (30 m, 2.3)

Figure 13 shows the drag oscillation for each of the barriers, which increases in amplitude with barrier width, compared with the two-dimensional case. The variation in the wave amplitude is so large in the two-dimensional case that wave breaking is seen in the wave troughs, although none was observed in any of the three-dimensional cases at this Reynolds number. The results of the multigrid performance are summarised in Table V for the widest of the three barriers where grid-independent convergence is obtained. The gains from the multigrid compare well with the corresponding factors of 6.7 and 4.6 on two-dimensional grids of size 400×80 with the same two sizes of the time step.

The second case demonstrated is high Reynolds number flow past the set of three smooth cosine-shaped obstacles described earlier. The computations described here were undertaken with $F_h = 0.7$ and realism was enhanced by increasing the domain height to $D/h = 10$ (so that $K = 4.55$). The finest grid contained $160 \times 40 \times 40$ cells and covered $-50 \le x/h \le 25$, $0 \le y/h \le 8$, and $0 \le z/h \le 10$, with the upstream boundary sufficiently far away to allow computation up until approximately $Ut/h = 23$ before reflections return to the region of interest. The Reynolds number is taken to be $\mathrm{Re} = 10^5$ and mixing length turbulence model mentioned in the Introduction is used.

The interaction of a density-stratified fluid with a smooth three-dimensional obstacle is complex, with precise behavior determined by the value of the Froude number and the obstacle shape. Amplitudes of downstream lee waves generally increase with spanwise obstacle width, and the effect of the obstacle width on the occurrence of wave breaking at this Froude number is shown in Fig. 14, where streamlines in the centre and bottom planes are plotted for the widest obstacle at $Ut/h = 20$. The amplitude over the two narrower obstacle is too small for wave-breaking to occur, and these qualitative features agree with experimental data [44]. The multigrid convergence data are summarised in Table VI for the computations on the finest grid with each obstacle. As in the steady cases the amount of work required increases with obstacle width, and although the speedup factors are less than those for the unsteady laminar case discussed above, they are still worthwhile, particularly for the larger time step.

5. CONCLUSIONS

The equations arising from a staggered grid finite volume discretisation of the Navier–Stokes equations have been solved using a multigrid method. A variety of flow conditions in two and three dimensions have been considered, including neutral and stable density stratification, steady and unsteady flow, low and high Reynolds number, and Cartesian or curvilinear geometry, and examples have been given demonstrating the range of capability of the algorithm.

The asymptotic convergence rate of the multigrid process when used to compute steady stratified flow has been found to depend on the nature of the flux limiter used for the density, when this equation is convection-dominated, and occasionally the velocities also. For the cases and parameters tried a piecewise linear limiter function performed much better than fully nonlinear limiters. Although further work is perhaps required to fully resolve the issue, this is currently attributed to the presence of the high-order terms in the right-hand side of the coarse grid equations which remove the guarantee of convergence when these terms are nonlinear.

The implementation of the multigrid algorithm has been extended to deal with flows past three-dimensional obstacles and has been demonstrated in the computation of neutral and stably stratified flow past a set of vertical barriers of increasing width. The search for the most efficient solver for three-dimensional flows is an important issue, however, and future work should include comparisons with other smoothers such as DGS [21], more recent line smoothers [17], and genuine planewise smoothers.

The SIMPLE smoother was used to compute steady flow over the vertical barriers under conditions of increasing density stratification, when for weakly stratified flow ($K < 1$) the separation length and obstacle drag decreased in accordance with experimental observations. For these cases a grid-dependent underrelaxation strategy was adopted, where smaller underrelaxation factors were required when solving the equations on the coarsest grid than when merely smoothing the solution on the other grids in the sequence. The amount of work required to solve the problem generally increased with increasing stratification and obstacle width.

Finally, some indications have been given regarding the effectiveness of the multigrid algorithm when used to simulate three-dimensional unsteady flows under conditions of strong stratification ($K > 1$). Results of the computation on the finest grid of laminar flow over the vertical barriers suggest significant speedup factors over the corresponding single-grid computation case, although these tend to be smaller in the case of high Reynolds number flow over smooth topography. Initial results are encouraging, however, and warrant further investigation. It already appears clear that the study of unsteady phenomena associated with incompressible density-stratified flow past three-dimensional obstacles, such as wave breaking and vortex shedding, could be undertaken with the reasonable expectation that the multigrid algorithm would contribute a useful reduction in the computing time required; see [45], for example.

APPENDIX

The mapping from Cartesian (x, y, z) to curvilinear coordinates (ξ, η, ζ) is Clark's [46] terrain-following transformation and used in Apsley [47], for example. For a domain of depth D and a lower surface given by $z_s(x, y)$ we have

$$\begin{aligned} \xi &= x \\ \eta &= y \\ \zeta &= \frac{z - z_s(x, y)}{1 - z_s(x, y)/D}. \end{aligned}$$

Derivatives transform according to

$$\frac{\partial}{\partial x} = \frac{\partial}{\partial \xi} - \frac{c_x}{\sqrt{g}}\frac{\partial}{\partial \zeta}$$
$$\frac{\partial}{\partial y} = \frac{\partial}{\partial \eta} - \frac{c_y}{\sqrt{g}}\frac{\partial}{\partial \zeta}$$
$$\frac{\partial}{\partial z} = \frac{1}{\sqrt{g}}\frac{\partial}{\partial \zeta},$$

where the Jacobian $\sqrt{g}$ and the two metric coefficients c_x, c_y are respectively given by

$$\sqrt{g} = 1 - z_s/D$$
$$c_x = \frac{1}{\sqrt{g}}(1 - \zeta/D)\frac{\partial z_s}{\partial x}$$
$$c_y = \frac{1}{\sqrt{g}}(1 - \zeta/D)\frac{\partial z_s}{\partial y}.$$

Each of the equations for momentum (1) or density transport (3) can be written in generic conservation form as

$$\frac{\partial}{\partial t}(\varphi) + \frac{\partial}{\partial x}\left(u\varphi - \Gamma\frac{\partial \varphi}{\partial x}\right) + \frac{\partial}{\partial y}\left(v\varphi - \Gamma\frac{\partial \varphi}{\partial y}\right) + \frac{\partial}{\partial z}\left(w\varphi - \Gamma\frac{\partial \varphi}{\partial z}\right) = S,$$

where S is a source term. Under the coordinate transformation this becomes

$$\frac{\partial}{\partial t}(\sqrt{g}\varphi) + \frac{\partial}{\partial \xi}\left[\sqrt{g}u\varphi - \sqrt{g}\Gamma\frac{\partial \varphi}{\partial \xi} + c_x\Gamma\frac{\partial \varphi}{\partial \zeta}\right] + \frac{\partial}{\partial \eta}\left[\sqrt{g}v\varphi - \sqrt{g}\Gamma\frac{\partial \varphi}{\partial \eta} + c_y\Gamma\frac{\partial \varphi}{\partial \zeta}\right]$$
$$+ \frac{\partial}{\partial \zeta}\left[(w - c_x u - c_y v)\varphi - \frac{1 + c_x^2 + c_y^2}{\sqrt{g}}\Gamma\frac{\partial \varphi}{\partial \zeta} + c_x\Gamma\frac{\partial \varphi}{\partial \xi} + c_y\Gamma\frac{\partial \varphi}{\partial \eta}\right] = \sqrt{g}S.$$

The discretisation of either of these leads to an equation of the form of (5). In each case the source term contains the pressure gradient, the buoyancy term if present, and the high-order part of the convective scheme. When the coordinate transformation is used, the discrete form of the mixed derivatives and additional pressure gradient terms are included in addition. The expanded forms in either case are those given by expressions (6)–(11).

The continuity equation (2) becomes

$$\frac{\partial}{\partial \xi}(\sqrt{g}u) + \frac{\partial}{\partial \eta}(\sqrt{g}v) + \frac{\partial}{\partial \zeta}(w - c_x u - c_y v) = 0.$$

For the SIMPLE method this is rewritten in terms of corrections to the velocities stored on the six faces which define a continuity control volume, with the current continuity residual on the right-hand side. The discrete equation is of the form

$$\left(u'_{i+1/2jk} - u'_{i-1/2jk}\right)\sqrt{g}\Delta A^{\xi}_{ijk}$$
$$+ \left(v'_{ij+1/2k} - v'_{ij-1/2k}\right)\sqrt{g}\Delta A^{\eta}_{ijk} + \left(w'_{ijk+1/2} - w'_{ijk-1/2}\right)\Delta A^{\zeta}_{ijk} = -R^{c}_{ijk}.$$

Truncated expressions for the velocity correction derived from the momentum equations (6)–(11) are substituted to derive a Poisson equation in the usual way.

ACKNOWLEDGMENTS

The author gratefully acknowledges the comments and suggestions for improvements made by referees at the review stage of this paper.

REFERENCES

1. A. J. Chorin, A numerical method for solving incompressible viscous flow problems, *J. Comput. Phys.* **2**, 275 (1967).
2. D. Drikakis, O. P. Iliev, and D. P. Vassileva, A nonlinear multigrid method for the three-dimensional incompressible Navier–Stokes equations, *J. Comput. Phys.* **146**, 301 (1998).
3. C. Liu, X. Zheng, and C. H. Sung, Preconditioned multigrid methods for unsteady incompressible flows, *J. Comput. Phys.* **139**, 35 (1998).
4. F. H. Harlow and J. E. Welch, *Phys. Fluids* **8**, 2182 (1965).
5. S. V. Patankar, A calculation procedure for two-dimensional elliptic situations, *Numer. Heat Transfer* **4**, 409 (1981).
6. S. W. Armfield, Ellipticity, accuracy and convergence of the discrete Navier–Stokes equations, *J. Comput. Phys.* **114**, 176 (1994).
7. S. Sivaloganathan and G. J. Shaw, On the smoothing properties of the SIMPLE pressure-correction algorithm, *Inter. J. Num. Methods Fluids* **8**, 441 (1988).
8. K. M. Smith, W. K. Cope, and S. P. Vanka, A multigrid procedure for three-dimensional flows on non-orthogonal collocated grids, *Int. J. Numer. Methods Fluids* **17**, 887 (1993).
9. F. S. Lien and M. A. Leschziner, Multigrid acceleration for turbulent flow with a non-orthogonal collocated scheme, *Comput. Methods Appl. Mech. Eng.* **118**, 351 (1994).
10. M. F. Paisley, Multigrid computation of stratified flow over two-dimensional obstacles, *J. Comput. Phys.* **136**, 411 (1997).
11. C. W. Lan and M. C. Liang, Multigrid methods for incompressible heat flow problems with an unknown interface, *J. Comput. Phys.* **152**, 55 (1999).
12. P. Tamamidis, G. Zhang, and D. N. Assanis, Comparison of pressure-based and artificial compressibility methods for solving 3D steady incompressible viscous flows, *J. Comput. Phys.* **124**, 1 (1996).
13. D. Kwak, C. Kiris, and J. Dacles-Mariani, An assessment of artificial compressibility and pressure projection methods for incompressible flow simulations, in *16th International Conference on Numerical Methods in Fluid Dynamics*, edited by C. H. Bruneau Lecture Notes in Physics (Springer-Verlag, Heidelberg, 1998), Vol. 515, pp. 177–182.
14. S. P. Vanka, Block implicit multigrid solution of the Navier–Stokes equations in primitive variables, *J. Comput. Phys.* **65**, 138 (1986).
15. S. P. Vanka, A calculation procedure for three-dimensional steady recirculating flows using multigrid methods, *Comput. Methods Appl. Mech. Eng.* **55**, 321 (1986).
16. S. Zeng and P. Wesseling, Numerical study of a multigrid method with four smoothing methods for the incompressible Navier–Stokes equations in general coordinates, in *Sixth Copper Mountain Conference on Multigrid Methods*, edited by N. D. Melson, T. A. Monteuffel, S. F. McCormick, and C. C. Douglas (NASA Conference Publication 3339, 1996), pp. 409–424.
17. C. W. Oosterlee, F. J. Gaspar, T. Washio, and R. Wienands, Multigrid line smoothers for higher order upwind discretisations of convection-dominated problems, *J. Comput. Phys.* **139**, 274 (1998).
18. S. Zeng, C. Vuik, and P. Wesseling, Numerical solution of the incompressible Navier–Stokes equations by Krylov subspace and multigrid methods, *Adv. Comput. Math.* **4**, 27 (1995).

19. J. Piquet and X. Vasseur, Multigrid preconditioned Krylov subspace methods for three-dimensional numerical solutions of the incompressible Navier–Stokes equations, *Numer. Algorithms* **17**, 1 (1998).
20. C. W. Oosterlee, A GMRES-based plane smoother in multigrid to solve 3D anisotropic fluid flow problems, *J. Comput. Phys.* **130**, 41 (1997).
21. A. Brandt and N. Dinar, in *Numerical Methods for Partial Differential Equations*, edited by S. Parter (Academic Press, New York/London, 1979), p. 53.
22. A. Brandt and I. Yavneh, On multigrid solution of high-Reynolds incompressible entering flow, *J. Comput. Phys.* **101**, 151 (1992).
23. A. Brandt, Guide to multigrid development, in *Multigrid Methods*, edited by W. Hackbusch and U. Trottenberg Lecture Notes in Mathematics (Springer-Verlag, Berlin, 1982), Vol. 260.
24. M. F. Paisley and N. M. Bhatti, Comparison of multigrid methods for neutral and stably-stratified flows over two-dimensional obstacles, *J. Comput. Phys.* **142**, 581 (1998).
25. S. Sivaloganathan, G. J. Shaw, T. M. Shah, and D. F. Mayers, A comparison of multigrid methods for the incompressible Navier–Stokes equations, in *Numerical Methods for Fluid Dynamics*, edited by K. W. Morton and M. J. Baines (Oxford Univ. Press, London 1988), pp. 401–417.
26. C. H. Arakawa, A. O. Demuren, W. Rodi, and B. Schonung, Application of multigrid methods for the coupled and decoupled solution of the incompressible Navier–Stokes equations, in *Notes on Numerical Fluid Dynamics* (Vieweg, Wiesbaden 1988), Vol. 20, pp. 1–8.
27. M. F. Paisley, Multigrid solution of the incompressible Navier–Stokes equations for three-dimensional re-circulating flow: Coupled and decoupled smoothers compared, *Int. J. Numer. Methods Fluids* **30**, 441 (1999).
28. I. P. Castro, W. H. Snyder, and P. G. Baines, Obstacle drag in stratified flow, *Proc. R. Soc. Lond. A* **429**, 119 (1990).
29. M. F. Paisley and I. P. Castro, A numerical study of wave-breaking in stratified flow over obstacle, *Dynam. Atmos. Oceans* **23**, 309 (1996).
30. H. Hanazaki, Drag coefficient and upstream influence in three-dimensional stratified flow of finite depth, *Fluid Dynam. Res.* **4**, 317 (1989).
31. C. Schar and D. R. Durran, Vortex formation and vortex shedding in continuously stratified flows past isolated topography, *J. Atmos. Sci.* **54**, 534 (1997).
32. P. Wesseling, A. Segal, and C. G. M. Kassels, Computing flows on general three-dimensional nonsmooth staggered grids, *J. Comput. Phys.* **149**, 333 (1999).
33. B. van Leer, Upwind-difference methods for aerodynamics problems governed by the Euler equations, in *Large Scale Computations in Fluid Mechanics*, edited by B. Enquist, S. Osher, and R. Somerville, Lectures in Applied Mathematics (Amer. Math. Soc., Providence, RI, 1985), Vol. 22, II, p. 327.
34. B. P. Leonard and S. Mokhtari, Beyond first-order upinding: The ultra-sharp alternative for non-oscillatory steady state simulation of convection, *Int. J. Numer. Methods Eng.* **30**, 729 (1990).
35. P. Wesseling, M. Zijlema, A. Segal, and C. G. M. Kassels, Computation of turbulent flow in general domains, *Math. Comput. Sim.* **44**, 369 (1997).
36. P. K. Sweby, High resolution schemes using flux limiters for hyperbolic conservation laws, *SIAM J. Numer. Anal.* **21**(5), 995 (1984).
37. B. Van Leer, Towards the ultimate conservative difference scheme II. Monotonicity and conservation combined in a second order scheme, *J. Comput. Phys.* **14**, 361 (1974).
38. Ch. Hirsch, Numerical Computation of Internal and External Flows (Wiley, Chichester, 1990), Vol. 2.
39. R. M. Smith and A. G. Hutton, The numerical treatment of advection: A performance comparison of current methods, *Numer. Heat Transfer* **5**, 439 (1982).
40. J. Caspar and M. H. Carpenter, Computational considerations for the simulation of shock-induced sound, *SIAM J. Sci. Comput.* **19**(3), 813 (1998).
41. M. H. Carpenter and J. Caspar, Accuracy of shock capturing in two spatial dimensions, *AIAA J.* **37**(9), 1072 (1999).
42. K. G. Lamb, Numerical simulations of stratified inviscid flow over a smooth obstacle, *J. Fluid Mech.* **260**, 1 (1994).

43. J. W. Rottmann, D. Broutman, and R. Grimshaw, Numerical simulations of uniformly-stratified fluid flow over topography, *J. Fluid Mech.* **306**, 1 (1996).
44. I. P. Castro and W. H. Snyder, Experiments on wave-breaking in stratified flow over obstacles, *J. Fluid Mech.* **255**, 195 (1993).
45. I. P. Castro, S. Vosper, M. F. Paisley, and P. Hayden, Vortex shedding behind tapered obstacles in neutral and stratified flow, *Dynamics of Atmospheres and Oceans*, to appear.
46. T. L. Clark, A small-scale dynamic model using a terrain-following coordinate transformation, *J. Comput. Phys.* **24**, 186 (1977).
47. D. D. Apsley and I. P. Castro, Flow and dispersion over hills: Comparison between numerical predictions and experimental data, *J. Wind Eng. Ind. Aer.* **67**, 375 (1997).